

## High Temperature Corrosion Behavior of Ni-Based Alloys

Soo-Haeng Cho<sup>1,\*</sup>, Seung-Chul Oh<sup>1</sup>, Seong-Bin Park<sup>1</sup>, Kwang-Mo Ku<sup>2</sup>, Jong-Hyeon Lee<sup>2,3,\*</sup>,  
Jin-Mok Hur<sup>1</sup>, and Han-Soo Lee<sup>1</sup>

<sup>1</sup>Korea Atomic Energy Research Institute, 989-111 Daedeokdae-ro, Yuseong-gu, Daejeon 305-353, Korea

<sup>2</sup>Graduate School of Department of Metal Engineering, Chungnam National University,

79 Daehak-ro, Yuseong-gu, Daejeon 305-764, Korea

<sup>3</sup>Graduate School of Green Energy Technology, Chungnam National University,

79 Daehak-ro, Yuseong-gu, Daejeon 305-764, Korea

(received date: 26 July 2011 / accepted date: 19 January 2012)

The high temperature corrosion behavior of N07263, N06600, and N06625 in LiCl-Li<sub>2</sub>O molten salt was investigated at temperatures ranging from 650 to 850 °C in a glove box. The high temperature corrosion behavior was observed using measurements of the oxide morphology and thickness, the extent of internal corrosion, and the compositional changes in the scale and in the substrate. Corrosion tests were performed, and these demonstrated that the main corrosion products were Fe(Ni,Co)<sub>3</sub>, FeNi<sub>3</sub>, and LiCrO<sub>2</sub>. The internal corrosion of N07263 was localized, while that of N06600 maintained intergranular corrosion throughout the test temperature range. N06625 exhibited uniform intergranular corrosion behaviors at low and high temperatures. N07263 exhibited superior corrosion resistance, as evidenced by its corrosion layer which was more continuous, dense, and adherent when compared with those of N06600 and N06625.

**Key words:** alloys, corrosion, scanning electron microscopy (SEM), electrolytic reduction

### 1. INTRODUCTION

Molten salt technology has been widely applied in industrial applications due to its highly desirable physical and chemical characteristics, such as high electrical conductivities, high processing rates, and desirable fluid characteristics. However, molten salts may cause corrosion to the container materials and to various components of electrolysis equipment. Hence, numerous studies have been conducted on the corrosion of the structural materials that are used for handling high temperature molten salts, such as sulfates [1-4], carbonates [5-7], and chloride systems [8-11]. Ni-based superalloys have been developed for high temperature applications due to their excellent resistance to corrosion at elevated temperatures, such as those encountered when handling lithium molten salt (LiCl-Li<sub>2</sub>O). Therefore, these Ni-based alloys are used in applications for molten salt and are exposed to elevated temperatures. High temperature corrosion testing in the lithium molten salt is considered very important for material characterization and for the performance ranking of high temperature applications of such materials. Although several studies have been conducted on the high temperature corrosion

behavior of Ni-based alloys in different types of environments [12-17], there have been few reports on their high temperature corrosion in lithium molten salt, which is the subject of this research.

In the present study, the electrolytic reduction of a spent oxide nuclear fuel, which was performed in a lithium molten salt at 650 °C, was simulated to test the corrosion behavior of several commercially available structural materials. The liberation of oxygen at the anode and the resulting high temperature molten salts created a chemically aggressive environment that is severely corrosive for ordinary structural materials [18,19]. Therefore, there is a clear need for the development of corrosion-resistant materials that can be employed in this type of electrolytic reduction technology. The N07263, N06600, and N06625 alloys were selected as candidate materials due to their excellent mechanical properties and corrosion resistance in high temperature conditions; their high temperature corrosion behavior was investigated under simulated electrolytic reduction conditions.

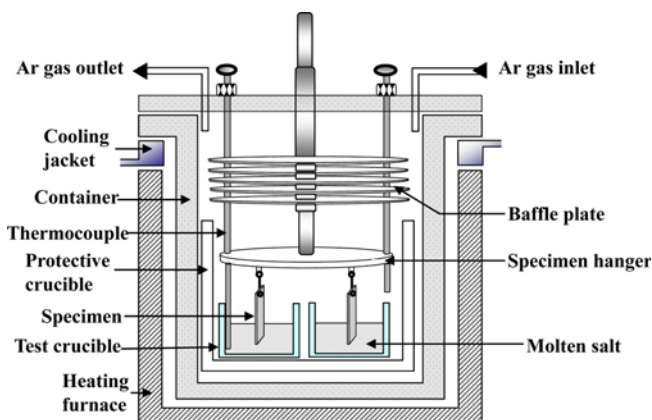
### 2. EXPERIMENTAL PROCEDURES

The present research was conducted using three Ni-based superalloys: N07263, N06600, and N06625. Their chemical compositions are listed in Table 1. Specimens with dimensions

\*Corresponding author: nshcho1@kaeri.re.kr, jonglee@cnu.ac.kr  
©KIM and Springer, Published 20 December 2012

**Table 1.** Chemical compositions of the tested alloys (wt%)

Alloy (UNS No.)	Ni	Cr	Fe	C	Si	Mn	Mo	Nb	Al	Co	Ti
N07263	51.35	20.0	0.5	0.05	0.13	0.1	5.8	—	0.45	19.2	2.39
N06600	73.66	16.30	8.15	0.07	0.21	0.32	—	—	—	—	—
N06625	65.30	21.20	0.70	0.02	0.17	0.14	8.60	3.42	0.16	0.01	0.19

**Fig. 1.** Schematic diagram of the apparatus used for the corrosion tests.

of  $70 \times 15 \times 2$  mm were ground with grade 800 SiC paper, polished with diamond paste, and cleaned in a deionized water and acetone solution before being subjected to the high temperature corrosion tests.

The experimental apparatus is shown in Fig. 1. The lithium molten salt was introduced into a high density MgO crucible; then, it was heated to and maintained at  $300^\circ\text{C}$  for 3 h in an argon atmosphere in order to remove any moisture. When the desired temperature was reached, the specimens were immersed into the molten salt. The  $\text{Li}_2\text{O}$  concentration in LiCl was 1 wt%. The early corrosion behavior generally exhibits the protection ability of a material; thus, 72 h, which is the equivalent time for six batches of electrolytic reduction, was chosen as the duration of the corrosion test.

After the high temperature corrosion test, the specimens were removed from the salt and kept in a reactor under an argon gas atmosphere while the furnace was cooled to room temperature. Next, the reactor was opened and the specimens were removed and visually examined before being ultrasonically cleaned with deionized water, and the measurements were then taken. The total corrosion depth of a specimen exposed to the molten salt was defined as the depth to which the oxygen diffused through the specimen surface. The corroded specimens were cut using a diamond cutter and ultrasonically cleaned in acetone for characterization purposes. Then, they were cold-mounted, ground, and polished to prepare them for metallographic examination. The microstructure, morphology, and chemical composition of the surface and of the cross section were examined using a scanning electron microscope (SEM; JSM-6300, JEOL, Japan) equipped with an energy dispersive spectrometer

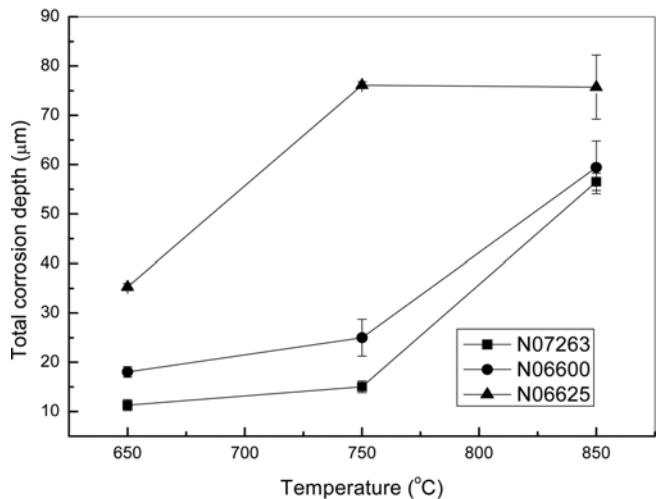
(EDS). An X-ray diffraction (XRD; DMAX/1200, Rigaku, Japan) was used to determine the structure of the corrosion products, and their thermodynamical stabilities were calculated using HSC Chemistry 6.1® in order to understand the formation mechanism [20].

### 3. RESULTS AND DISCUSSION

#### 3.1. Total corrosion depth measurements

The corrosion depths of N07263, N06600, and N06625 after the high temperature corrosion tests in LiCl-1% $\text{Li}_2\text{O}$  molten salt at temperatures between  $650$  and  $850^\circ\text{C}$  are shown in Fig. 2. These depths ranged from  $11.32\text{ }\mu\text{m}$  to  $76.11\text{ }\mu\text{m}$  for the studied alloys, with N07263 and N06625 exhibiting the lowest and highest corrosion depths, respectively. The corrosion layer thickness of N07263 and N06600 slightly increased until the temperature reached  $750^\circ\text{C}$ , after which it linearly increased for temperatures between  $750$  and  $850^\circ\text{C}$ . For N06625, the corrosion layer thickness linearly increased until the temperature reached  $750^\circ\text{C}$  and almost no change was observed between  $750$  and  $850^\circ\text{C}$ .

These differences in the corrosion depth for the three specimens, which are shown in Fig. 2, were attributed to the formation of the outer corrosion layer and to the internal corrosion, which leads to a slight spallation from the base metal surface as well as dissolution of the scales and other corroded products [21]. Therefore, it was assumed that the formation of the corrosion layer and its adherence to the base metal significantly influenced the corrosion depth.

**Fig. 2.** Total corrosion depth as a function of temperature for the three alloys corroded for 72 h.

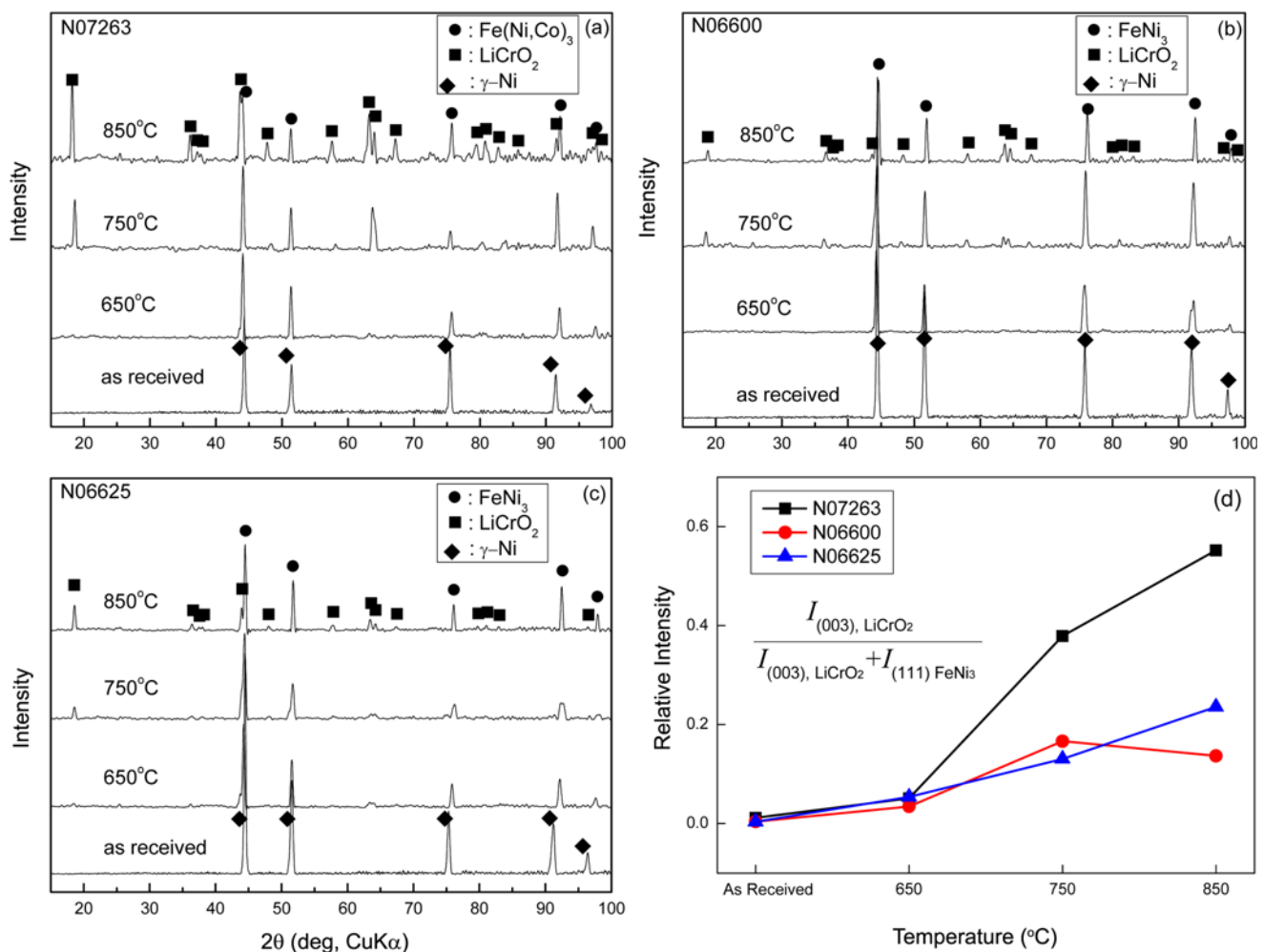
### 3.2. Corrosion products analysis

Figure 3 shows the XRD patterns both for the corrosion products formed on the specimen surface after the high temperature corrosion tests and for the initial, un-corroded specimens. The results demonstrate that the initial phase of the investigated alloys was a single phase of  $\gamma$ -Ni that formed due to the high solubility of the alloying elements in Ni. For N07263 (Fig. 3(a)), the diffraction pattern of the specimen shifted to the angle of  $\text{Fe}(\text{Ni},\text{Co})_3$  at temperatures above 650 °C. It is assumed that the Fe diffused to the surface and then formed an intermetallic phase with Ni. However, there are only limited data available on the stability of Fe-Ni compounds, especially at elevated temperatures. Tendler *et al.* reported that  $\text{FeNi}_3$  is the most stable phase between  $\text{Fe}_3\text{Ni}$ ,  $\text{FeNi}$ , and  $\text{FeNi}_3$  at room temperature and that  $\gamma$  Fe-Ni solid solution (Ni-rich) is more stable than  $\alpha$  Fe-Ni solid solution (Fe-rich) at 625 and 725 °C [22]. It should be noted that a new phase, identified as  $\text{LiCrO}_2$ , appeared at 750 °C and that its fraction increased at 850 °C.

Generally, the corrosion resistance of a metallic material is enhanced when a dense and continuous oxide layer is formed onto its surface. A similar forming procedure of a  $\text{LiCrO}_2$  phase was observed in N06600 and N06625 (Figs. 3(b) and 3(c), respectively), but the intensity of the  $\text{LiCrO}_2$  peak for these two alloys was lower than that of N07263. This may be the primary reason for the corrosion resistance of N07263 being superior compared with the other samples, as shown in Fig. 2. The relative intensity of the  $\text{LiCrO}_2$  to  $\text{FeNi}_3$  was calculated using Eq. (1) based on the XRD results, which are depicted in Fig. 3(d).

$$\text{Relative intensity of LiCrO}_2 = \frac{I_{(003),\text{LiCrO}_2}}{I_{(003),\text{LiCrO}_2} + I_{(111),\text{FeNi}_3}}, \quad (1)$$

where  $I_{(003),\text{LiCrO}_2}$  and  $I_{(111),\text{FeNi}_3}$  are the XRD intensities of the main peaks of (003) and (111) of  $\text{LiCrO}_2$  and  $\text{FeNi}_3$ , respectively. The relative intensity of  $\text{LiCrO}_2$  increased with the test temperature but it can be seen clearly in Fig. 3(d) that the fraction of  $\text{LiCrO}_2$  in N07263 was much higher than



**Fig. 3.** XRD patterns of the surface corrosion layer of (a) N07263, (b) N06600, and (c) N06625, and (d) the relative intensity between the (003) $_{\text{LiCrO}_2}$  and (111) $_{\text{FeNi}_3}$  peaks of the specimens corroded at 650 °C, 750 °C, and 850 °C for 72 h.

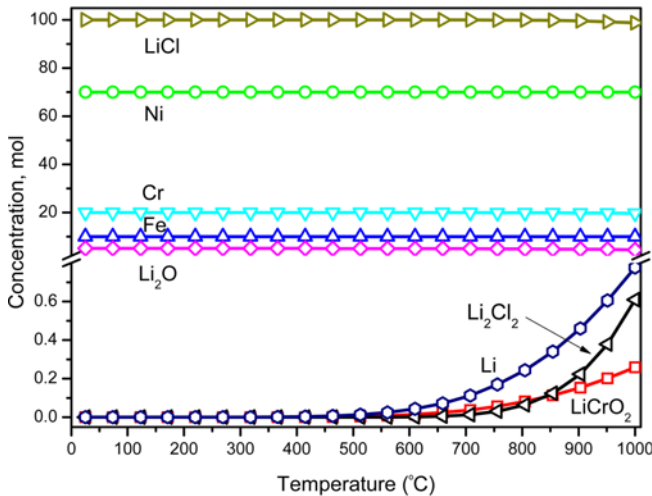


Fig. 4. Equilibrium composition of the alloying elements under the electrolyte environment at elevated temperatures (initial composition in mol: 100 LiCl, 5 Li<sub>2</sub>O, 70 Ni, 20 Cr, and 10 Fe).

that in N06600 and N06625.

In order to understand the formation of this protective oxide layer under the testing conditions, thermodynamic calculations were performed using the HSC Chemistry 6.1<sup>®</sup>

software [20] with 100 mol LiCl, 5 mol Li<sub>2</sub>O, 70 mol Ni, 20 mol Cr, and 10 mol Fe; the results are depicted in Fig. 4. The calculation results demonstrated that no chemical reaction occurred below 500 °C. However, the Li<sub>2</sub>Cl<sub>2</sub>, Li, and LiCrO<sub>2</sub> phases started to form after 550 °C and the intensities increased with temperature increases. The formation of Li<sub>2</sub>Cl<sub>2</sub> and free Li was not confirmed, probably due to their negligible amount, while LiCrO<sub>2</sub> was clearly detected as a corrosion product on the specimen's surface (see Fig. 3); this is in good agreement with the thermodynamical analysis results.

### 3.3. Corrosion behaviors

The cross sectional SEM images of the superalloys corroded at 650 to 850 °C in LiCl-1% Li<sub>2</sub>O molten salt were obtained in order to investigate the morphology of the corrosion layer and the internal corrosion, as shown in Fig. 5. The results suggest that the corrosion products formed on the specimen surface were almost intact because there was a negligible amount of corrosion precipitates in the molten salt after the test. However, it is clear that the morphology of the specimens changed significantly with the test temperature. At 650 °C, all alloy specimens presented a double corrosion

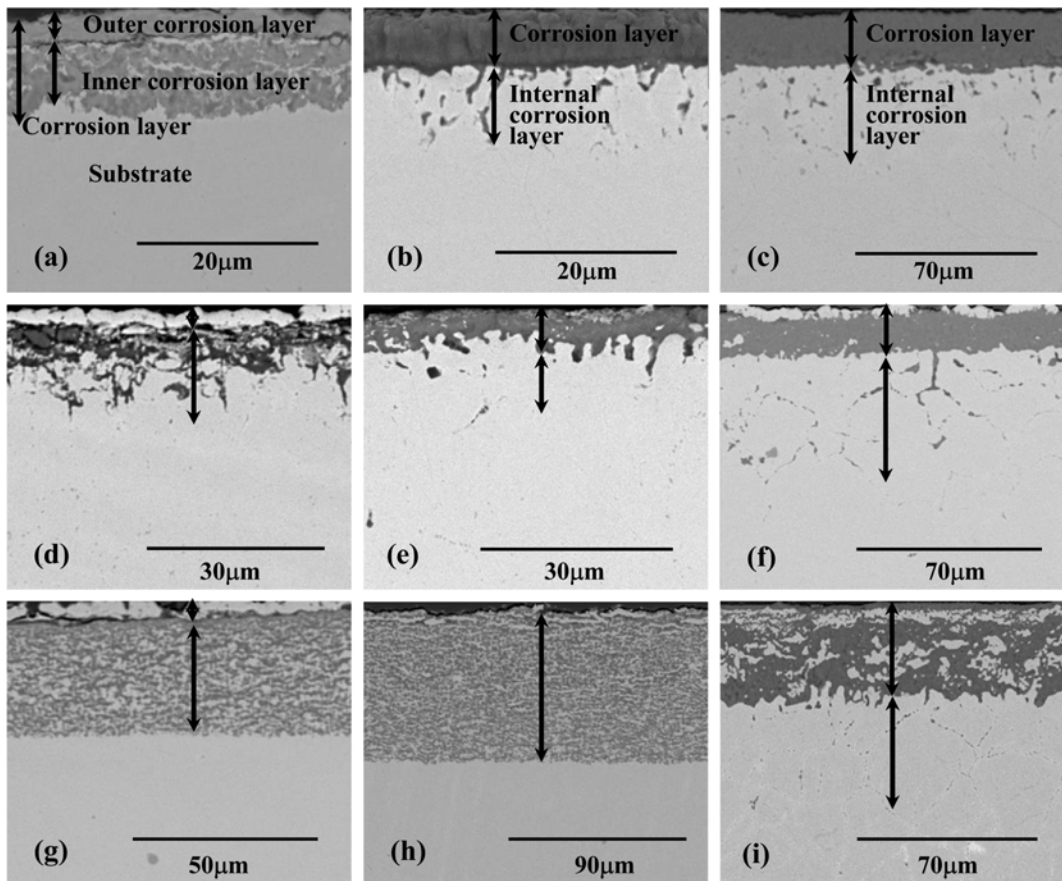
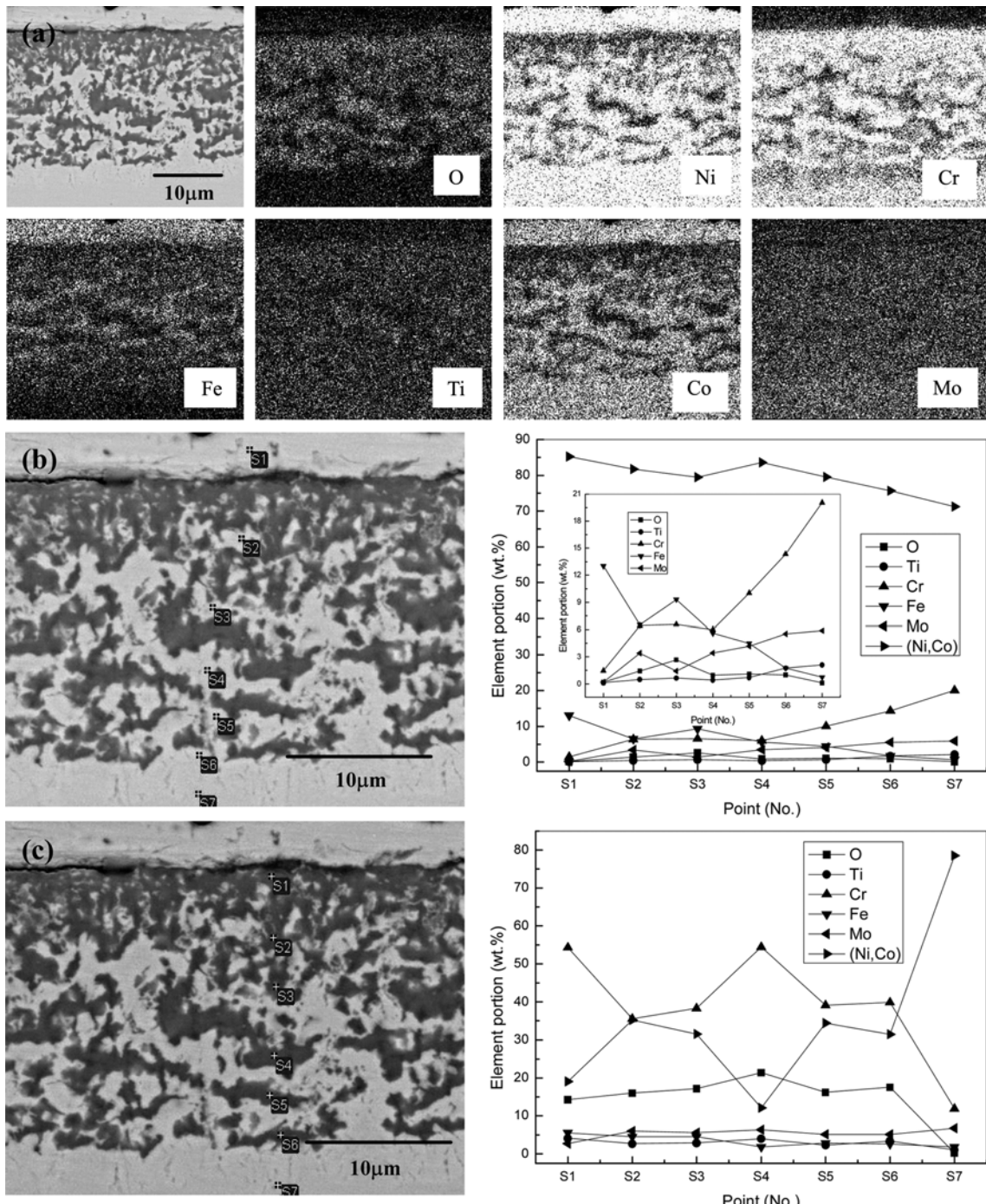


Fig. 5. Cross sectional SEM images of N07263 ((a) 650 °C, (b) 750 °C, and (c) 850 °C), N06600 ((d) 650 °C, (e) 750 °C, and (f) 850 °C), and N06625 ((g) 650 °C, (h) 750 °C, and (i) 850 °C) corroded for 72 h.

layer: a thin, white layer and an inhomogeneous inner layer. That is, an outer corrosion layer and an inner corrosion layer as indicated by the arrows in Figs. 5(a), 5(b), and 5(c). When the temperature increased to 750 °C, a dense and dark corrosion layer, with a thickness between 5 μm and 8 μm, was formed on the surface of the N07263 and N06600 specimens, while the thickness of the non-dark corrosion

layer increased to approximately 75 μm in N06625 (Figs. 5(b), 5(e), and 5(h)). The appearance of the dark corrosion layer at 750 °C was closely related to the stability of LiCrO<sub>2</sub>, as shown in Fig. 4. Furthermore, the thickness of LiCrO<sub>2</sub> phase increased as the temperature increased, which is in agreement with the XRD results (Fig. 3) and with the thermodynamic calculation results (Fig. 4).



**Fig. 6.** (a) Cross sectional microstructures and elemental maps, and ((b) and (c)) EDS point analysis results for N07263 corroded at 650 °C for 72 h (The superimposed graph presents a magnified area of a small portion of the element).

Figure 6 shows the cross sectional SEM images of (a) the elemental maps and (b and c) the point quantitative analysis results of N07263 corroded at 650 °C for 72 h. The outer corrosion layer of the specimen appeared to be composed of Fe(Ni,Co)<sub>3</sub>, which was detected using XRD and EDS analyses, as shown in Fig. 3(a) and Fig. 6(b), respectively, without an oxide phase, whereas a Cr oxide phase was observed beneath the outer corrosion layer through the elemental map and point quantitative analysis. Interestingly, an oxide

layer was formed beneath the intermetallic compound layer. One possible explanation for this is that the oxygen first diffused into the alloy matrix, giving rise to an oxygen-rich area, and then the alloying elements, such as Co and Fe, diffused out of the internal corrosion layer. The analysis of the depletion zone of Ni, Co, and Fe between the outer and inner corrosion layers, as shown in Fig. 6(a), appears to support this hypothesis.

The purpose of the point quantitative analysis was to

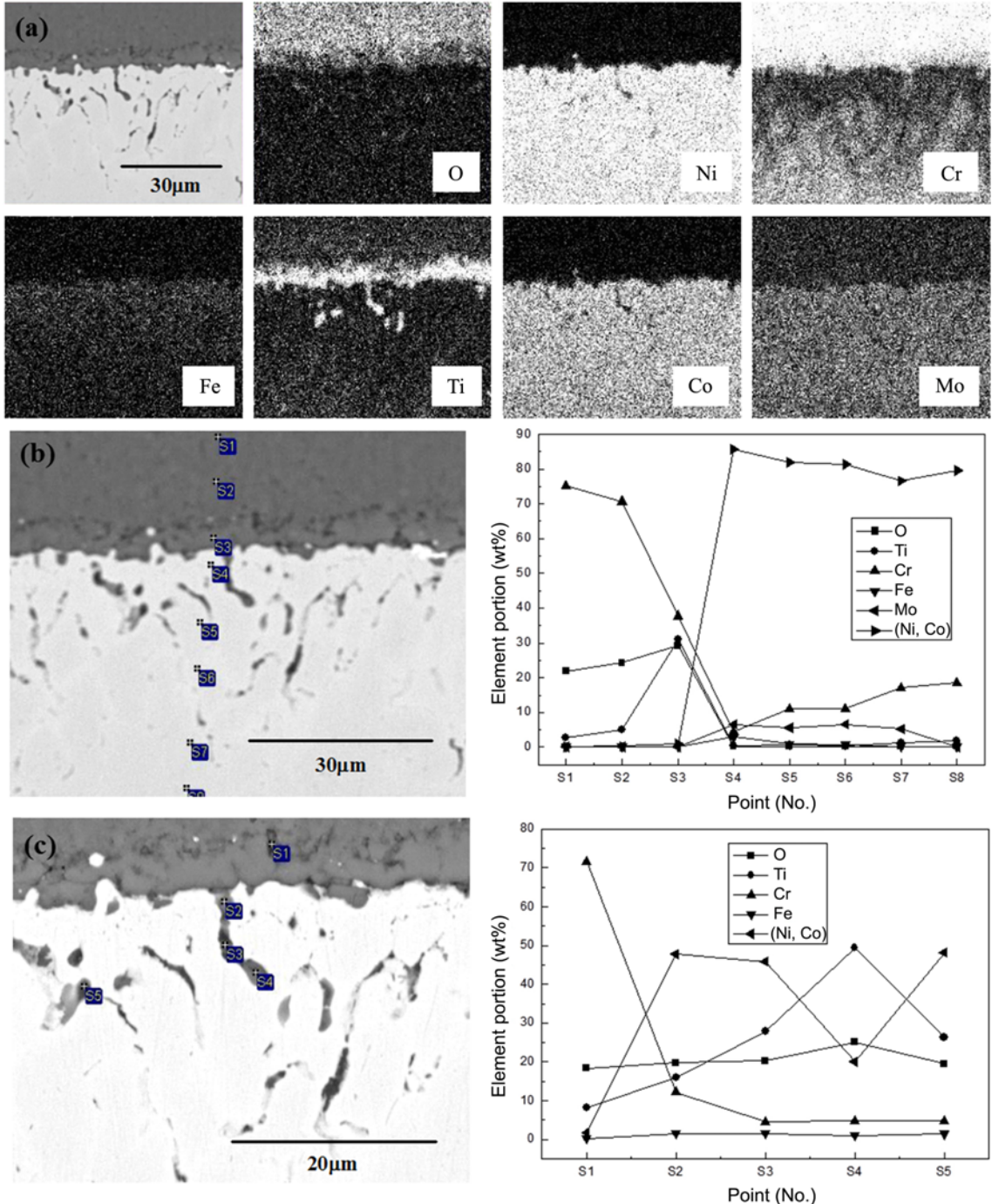


Fig. 7. (a) Cross sectional microstructures and elemental maps, and ((b) and (c)) EDS point analysis results for N07263 corroded at 850 °C for 72 h.

distinguish the metallic phase from the corrosion layer and to observe the distribution of the elements along the corrosion depth of the material. The obtained results demonstrated that the white-colored phase was a Ni-Co-Fe intermetallic compound and that the black-colored phase was primarily composed of Cr oxide, as shown in Figs. 6(b) and 6(c), respectively. Ti and Mo were found to be distributed in a relatively even manner throughout the corrosion layer, which implies that their diffusion was slower than that of the alloying elements such as Co, Cr, and Fe.

Figure 7 shows the cross sectional SEM images of (a) the elemental maps, (b) the cross sectional SEM image, and (c) the point quantitative analysis results of N07263 corroded at 850 °C for 72 h. It can be observed that the intermetallic compound layer, which was formed at 650 °C, was not detected at 850 °C and that a negligible amount of corrosion precipitates was found in the salt phase (Fig. 7(a)). It is believed that the thermodynamically stable LiCrO<sub>2</sub> phase was formed at the surface instead of the intermetallic compound phase. The Cr-rich corrosion layer was dense and continuous, meaning that it could retard the rapid corrosion reactions. Ti was

preferentially oxidized beneath the corrosion layer, thus being important in the corrosion layer formation [23]. The EDS point analysis results also showed that a Ti-rich oxide layer was formed beneath the corrosion layer, as shown in Figs. 7(b) and 7(c). It is well known that Ti, which has a strong affinity for oxygen, can prevent the oxidation of Ni-based superalloys because it is preferentially oxidized and that it passivates the underlying metal by forming its own oxide [24]. The Ti oxide could also have contributed to the corrosion resistance of N07263. The Ni-rich phase beneath the corrosion layer (S4 in Fig. 7(b)) is also believed to have been an effective barrier to the inward diffusion of the oxygen ions and the outward diffusion of the metal ions in the corroding environment [25].

Figure 8 shows the cross sectional SEM images of (a) the elemental maps and (b) the EDS point quantitative analysis result of N06600 corroded at 650 °C for 72 h. The outer corrosion layer was covered with a Ni-rich intermetallic compound (see Fig. 8(a)), such as FeNi<sub>3</sub>, whose formation is a phenomenon very similar to that observed in N07263, except that the inner corrosion layer in N06600 was com-

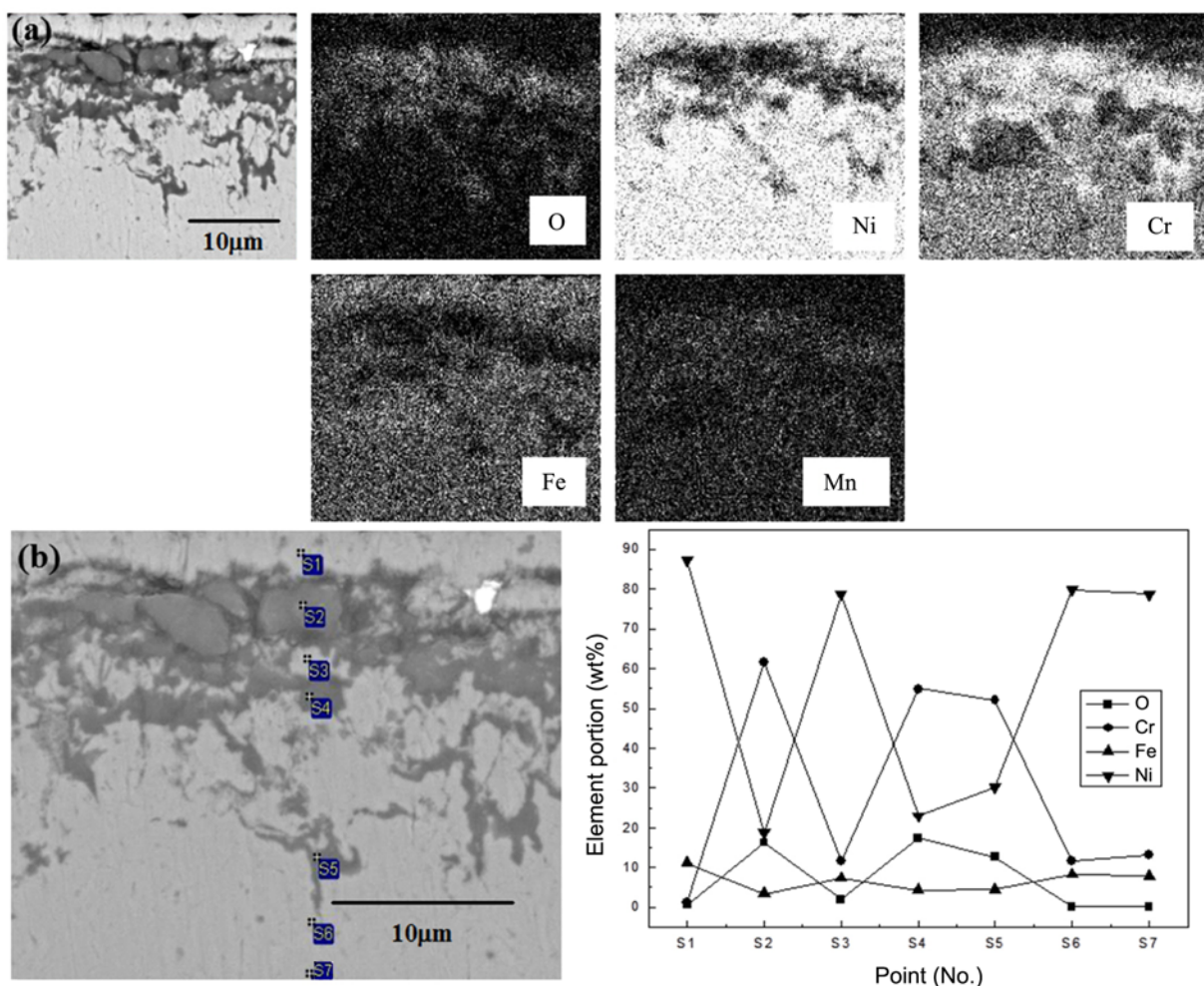
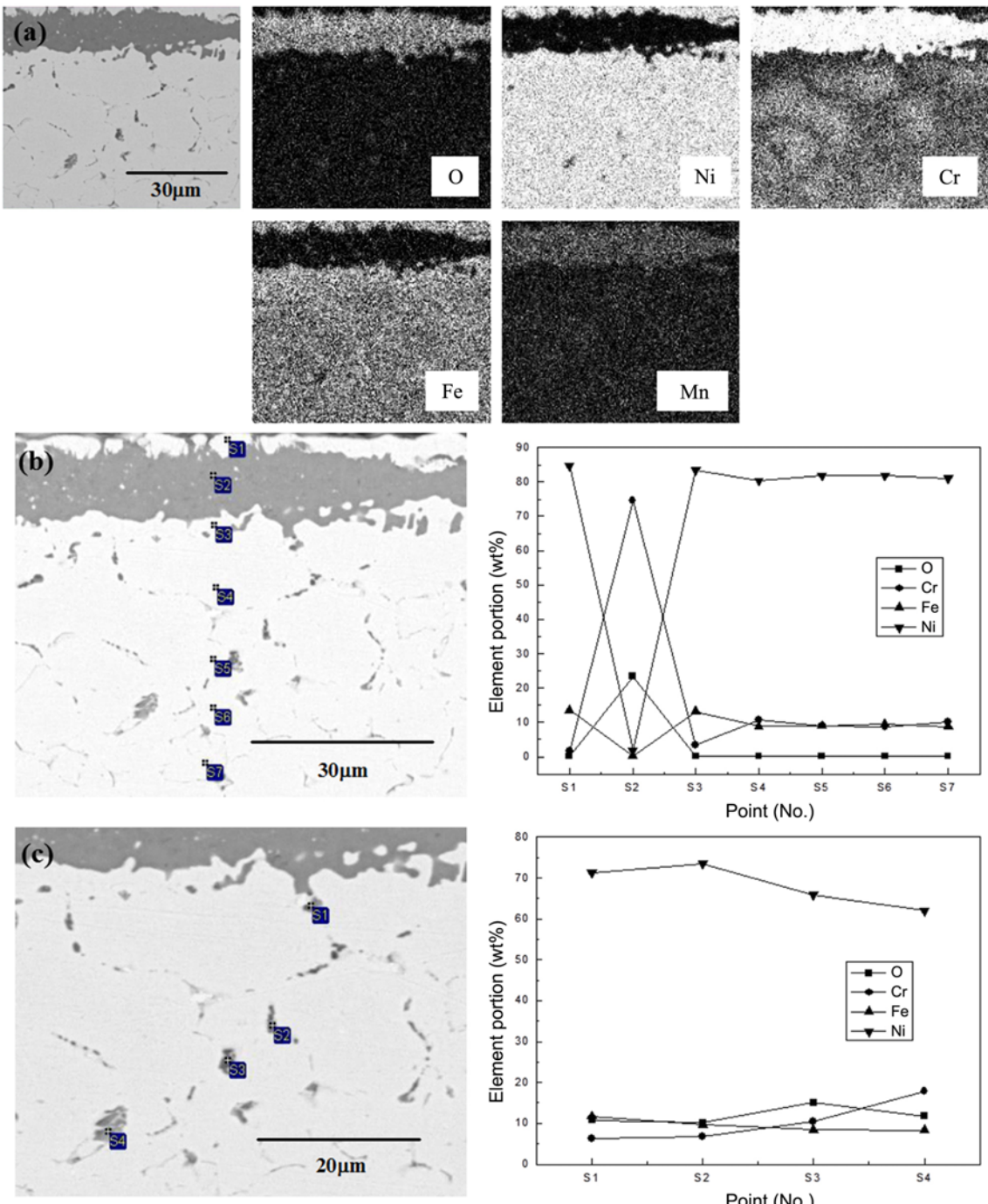


Fig. 8. (a) Cross-sectional microstructures and elemental maps, and (b) EDS point analysis results for N06600 corroded at 650 °C for 72 h.

posed of a discontinuous Cr oxide phase. The EDS point analysis results also demonstrated that the Cr oxide phase and Ni were randomly distributed in the inner corrosion layer, as shown in Fig. 8(b). Moreover, it was found that the inner corrosion behavior of N06600 exhibited typical intergranular corrosion to a large extent.

Figure 9 shows the cross sectional SEM images of (a) the elemental maps and ((b) and (c)) the EDS point quantitative

analysis results of N06600 corroded at 850 °C for 72 h. When the temperature was increased to 850 °C, the morphology of the corrosion layer of this alloy changed significantly as depicted in Fig. 9(a). The outer corrosion layer, composed of Ni-rich FeNi<sub>3</sub>, became thin and intermittent. The Cr-rich Mn oxide phase was predominantly observed beneath the outer corrosion layer, while the other elements were excluded from it. One of the most distinctive features in this sample



**Fig. 9.** (a) Cross sectional microstructures and elemental maps, and ((b) and (c)) EDS point analysis results for N06600 corroded at 850 °C for 72 h.

was that the oxygen concentration at the grain boundary was observed to be high when compared with that inside the granule (Figs. 9(b) and 9(c)). This is a direct indication of the intergranular corrosion and of the oxygen penetration, as the depth appeared to reach more than 50 mm, whereas a continuous oxide layer with a thickness of 16  $\mu\text{m}$  was formed at the surface. Hence, a higher corrosion rate was anticipated from the observed microstructural and compositional changes.

For N06625, which had the largest corrosion depth (as shown in Fig. 2), the corrosion layer presented a completely different microstructure. The cross sectional SEM image and the elemental maps of N06625 corroded at 650 °C demonstrated that the thickness of the inner corrosion layer was higher than 35  $\mu\text{m}$  and that the corrosion layer was evenly mixed with a Ni-rich Ni-Fe intermetallic phase and with a Cr oxide, as shown in Fig. 10(a). The individual phase

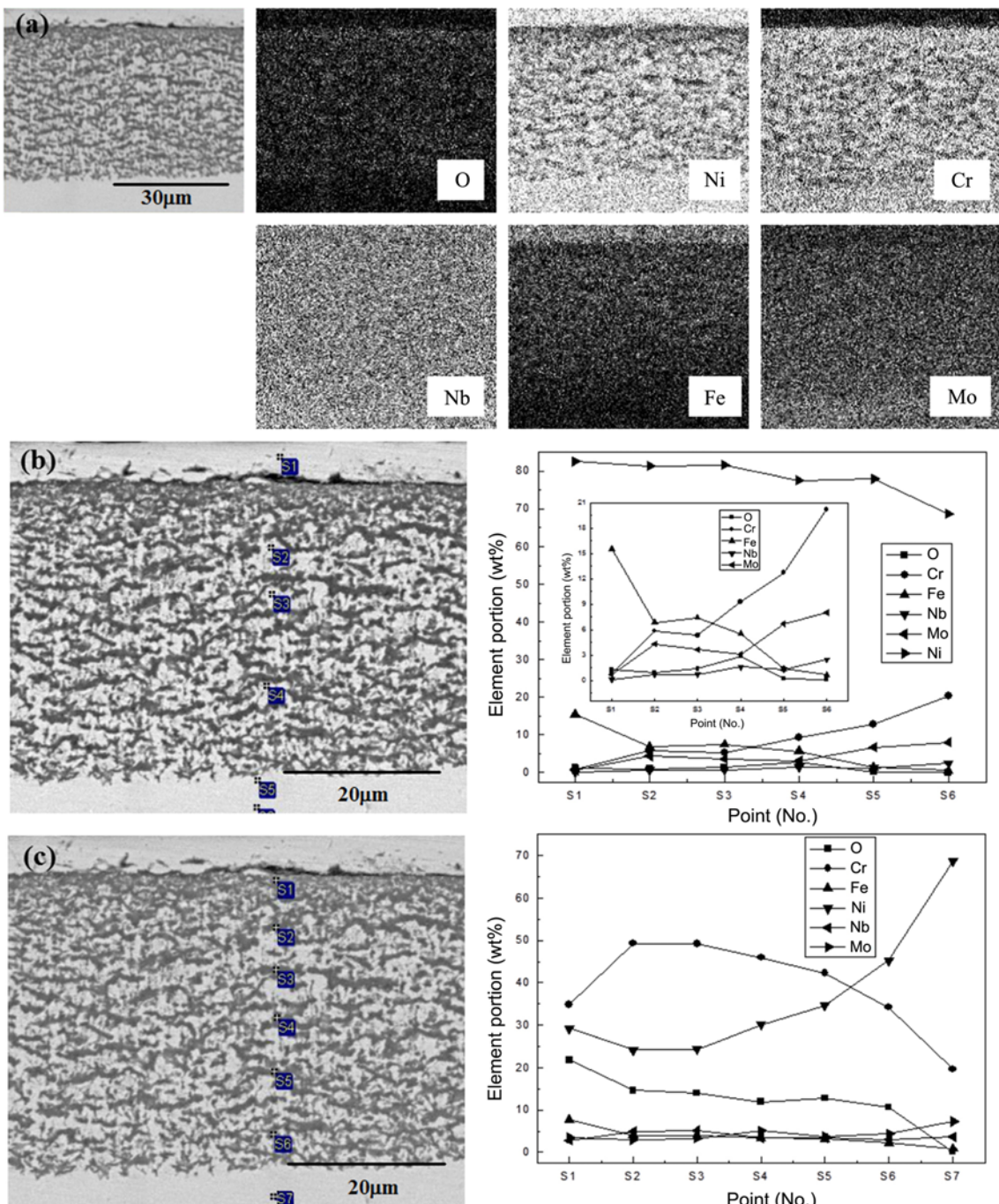


**Fig. 10.** (a) Cross sectional microstructures and elemental maps, and ((b) and (c)) EDS point analysis results for N06625 corroded at 650 °C for 72 h (The superimposed graph presents a magnified area of a small portion of the element).

in the inner corrosion layer was more closely analyzed through the EDS point quantitative analyses, and the results are presented in Figs. 10(b) and 10(c). The elemental distribution generally agreed with the image mapping presented in Fig. 10(a), and it should be noted that the observed Mo concentration was much lower than the substrate concentration, which was 8.6 wt%, (Figs. 10(b) and 10(c)). This may indicate that the role of Mo in enhancing the corrosion resistance was

limited when the LiCl-Li<sub>2</sub>O electrolyte was used at elevated temperatures, because Mo was not involved in the formation of the protective oxide layer. When the test temperature increased to 850 °C, the Ni-rich intermetallic compound was unevenly distributed in the Cr oxide phase, as shown in Fig. 11(a). Figure 11(b) demonstrates that the elemental distribution of the corrosion layer of N06625 was the most complex among the specimens corroded at 850 °C. It is well

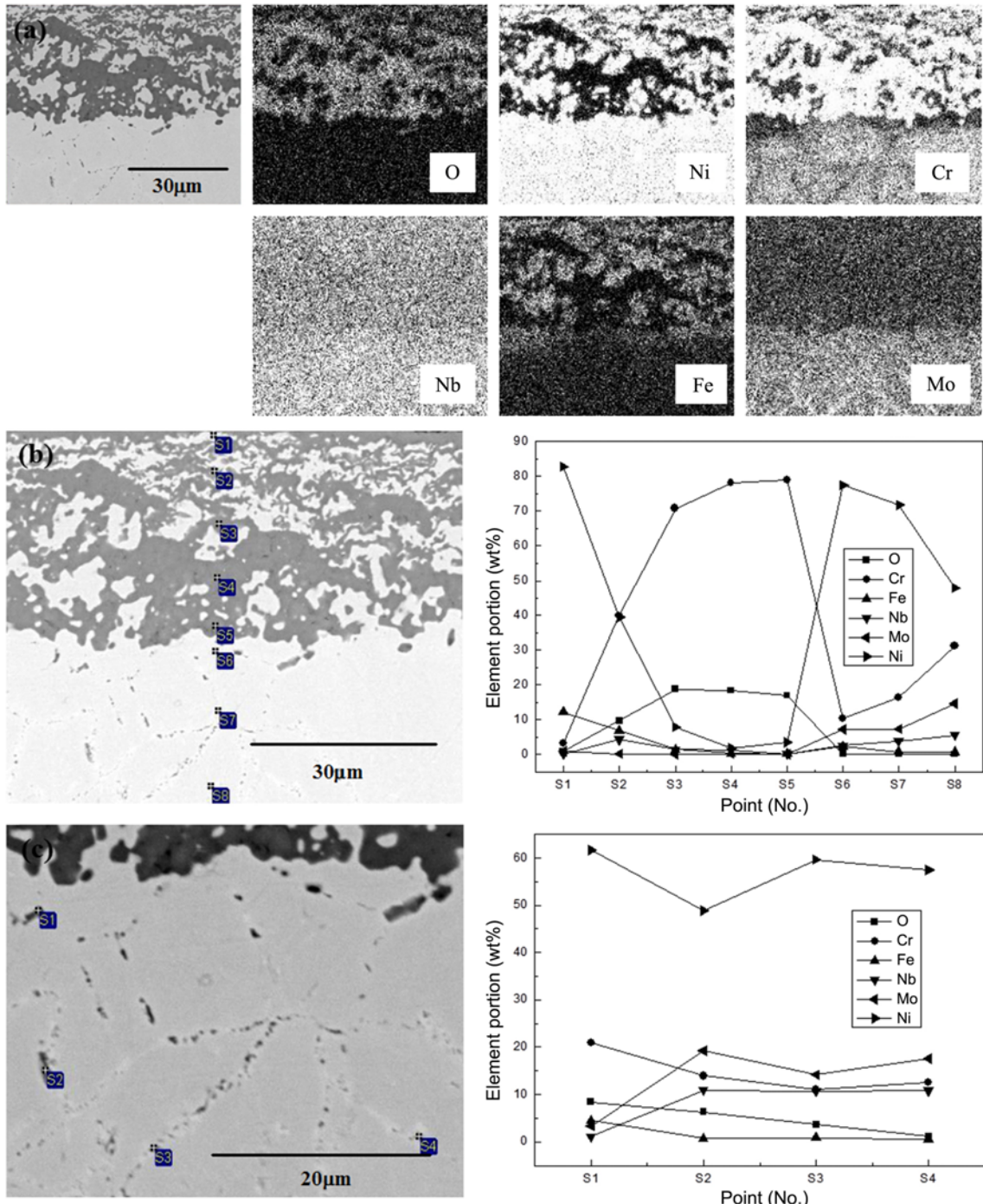


Fig. 11. (a) Cross sectional microstructures and elemental maps, and ((b) and (c)) EDS point analysis results for N06625 corroded at 850 °C for 72 h.

known that intergranular corrosion is usually characterized by extensive segregation of the oxides of alloying elements such as Mo, Cr, and Nb; this was confirmed through the EDS analysis, as presented in Fig. 11(c). Segregation causes depletion of the alloying elements in a grain and then causes the alloy to be prone to oxidation [26]. The series of experiments performed in this study clearly demonstrated that the superior corrosion resistance of N07263 (as compared with that of N06600 and N06625) at elevated temperatures was primarily due to the formation of a stable and dense protective oxide layer. In addition, Ti appeared to have a significant contribution in retarding the corrosion progress. This result can be useful in selecting the structural materials for the equipment used in the electrolytic reduction process.

#### 4. CONCLUSIONS

The corrosion behavior of the Ni-based superalloys was investigated in a high temperature corrosion environment. The total corrosion depth of the three commercial Ni-based superalloys varied in the order N07263 < N06600 < N06625, with N06625 having the highest corrosion depth. Among these alloys, N07263 exhibited superior corrosion resistance as a result of the formation of a protective oxide layer that was more continuous, dense, and adherent than that formed in the other two alloys. The primary corrosion products formed on the surface of the specimens were intermetallic  $\text{Fe}(\text{Ni},\text{Co})_3$ ,  $\text{FeNi}_3$ , and  $\text{LiCrO}_2$ . The internal corrosion behavior of N07263 exhibited localized corrosion throughout the test temperature range; N06600 exhibited intergranular corrosion, while the behavior of N06625 varied from uniform to intergranular corrosion with increases in the temperature. The corrosion resistance of the Ni-based superalloys in the lithium chloride molten salt in high temperature corrosion environments was strongly related to the phase composition of the materials. The experiments performed in this study demonstrated that the dense and continuous Cr-rich oxide layer retarded the progress of the corrosion process. Oxygen-active elements, such as Ti, formed oxide layers via preferential oxidation through their outward diffusion and prevented internal corrosion, which functioned as an interfacial barrier between the corrosion layer and the base metal.

#### ACKNOWLEDGMENTS

This work was funded by the National Mid- and Long-term Atomic Energy R&D Program, supported by the Ministry of Education, Science and Technology of Korea.

#### REFERENCES

1. A. Ruh and M. Spiegel, *Corros. Sci.* **48**, 679 (2006).
2. J. G. Gonzalez, S. Haro, A. Martinez-Villafane, V. M. Salinas-Bravo, and J. Porcayo-Calderon, *Mater. Sci. Eng. A* **435-436**, 258 (2006).
3. M. A. Uusitalo, P. M. J. Vuoristo, and T. A. Mantyla, *Corros. Sci.* **46**, 1311 (2004).
4. R. A. Rapp, *Corros. Sci.* **44**, 209 (2002).
5. M. Spiegel, P. Biedenkopf, and H. J. Grabke, *Corros. Sci.* **39**, 1193 (1997).
6. B. Zhu and G. Lindbergh, *Electrochim. Acta* **46**, 2593 (2001).
7. S. Mitsushima, N. Kamiya, and K. I. Ota, *J. Electrochem. Soc.* **137**, 2713 (1990).
8. T. Tzvetkov and J. Kolchakov, *Mater. Chem. Phys.* **87**, 201 (2004).
9. S. H. Cho, S. S. Hong, D. S. Kang, J. M. Hur, and H. S. Lee, *Met. Mater. Int.* **15**, 51 (2009).
10. B. P. Mohanty and D. A. Shores, *Corros. Sci.* **46**, 2893 (2004).
11. S. H. Cho, I. J. Cho, G. S. You, J. S. Yoon, and S. W. Park, *Met. Mater. Int.* **13**, 303 (2007).
12. B. R. Barnard, P. K. Liaw, R. A. Buchanan, and D. L. Klärstrom, *Mater. Sci. Eng. A* **527**, 3813 (2010).
13. F. Rabbani, L. P. Ward, and K. N. Strafford, *Oxid. Met.* **54**, 139 (2000).
14. F. A. Khalid and S. E. Benjamin, *Oxid. Met.* **54**, 63 (2000).
15. D. M. England and A. V. Virkar, *J. Electrochem. Soc.* **148**, A330 (2001).
16. J. H. Chen, P. M. Rogers, and J. A. Little, *Oxid. Met.* **47**, 381 (1997).
17. I. S. Kim, B. G. Choi, H. U. Hong, and C. Y. Jo, *Korean J. Met. Mater.* **49**, 535 (2010).
18. J. E. Indacochea, J. L. Smith, K. R. Litko, E. J. Karell, and A. G. Raraz, *Oxid. Met.* **55**, 1 (2001).
19. S. H. Cho, J. M. Hur, C. S. Seo, and S. W. Park, *J. Alloys Compd.* **452**, 11 (2008).
20. HSC Chemistry 6.12, Outotec Research Oy, Pori, Finland (2007).
21. M. H. Guo, Q. M. Wang, P. L. Ke, J. Gong, C. Sun, R. F. Huang, and L. S. Wen, *Surf. Coat. Technol.* **200**, 3942 (2006).
22. R. H. De Tendler, C. Rodriguez, L. J. Gallego, and J. A. Alonso, *Mater. Sci.* **31**, 6395 (1996).
23. E. T. Turkdogan, *Physical Chemistry of High Temperature Technology*, Academic Press, New York, (1980).
24. J. Stringer, *Mater. Sci. Eng. A* **120**, 129 (1989).
25. G. C. Wood, *Corros. Sci.* **2**, 173 (1962).
26. D. A. Jones, *Principles and Prevention of Corrosion*, Macmillan Publishing Company, New York (1992).